Non-canonical hedgehog pathway activation by MKL1/SRF promotes drug-resistance in basal cell carcinomas

Ramon J. Whitson[1], **Alex Lee**[2], **Nicole M. Urman**[1], **Amar Mirza**[1], **Catherine Y. Yao**[1], **Alexander S. Brown**[1], **Jiang R. Li**[1], **Gautam Shankar**[1], **Micah A. Fry**[1], **Scott X. Atwood**[1,3], **S. Tyler Hollmig**[1], **Sumaira Z. Aasi**[1], **Kavita Y. Sarin**[1], **Ervin H. Epstein Jr**[2], **Jean Y. Tang**[1], and **Anthony E. Oro**[1,4]

[1]Program in Epithelial Biology and Department of Dermatology, Stanford University School of Medicine Stanford, CA 94305 [2]Children's Hospital Oakland Research Institute, Oakland, CA [3]Department of Developmental and Cell Biology, University of California, Irvine, CA 92697

Abstract

Hedgehog pathway-dependent cancers can escape smoothened (SMO) inhibition through canonical pathway mutations, however, 50% of resistant BCCs lack additional variants in hedgehog genes. Here we use multi-dimensional genomics in human and mouse resistant BCCs to identify a non-canonical hedgehog activation pathway driven by the transcription factor, serum response factor (SRF). Active SRF along with its co-activator megakaryoblastic leukemia 1 (MKL1) form a novel protein complex and share chromosomal occupancy with the hedgehog transcription factor GLI1, causing amplification of GLI1 transcriptional activity. We show cytoskeletal activation by Rho and the formin family member Diaphanous (mDia) are required for SRF/MKL-driven GLI1 activation and tumor cell viability. Remarkably, we use nuclear MKL1 staining in mouse and human patient tumors to define drug responsiveness to MKL inhibitors highlighting the therapeutic potential of targeting this pathway. Thus, our studies illuminate for the first time cytoskeletal-driven transcription as a personalized therapeutic target to combat drug resistant malignancies.

INTRODUCTION

Targeted inhibition against causative oncogenic pathways in drug-naïve tumors provides a selective environment for outgrowth of drug-resistant clones[1]. Mutations causing drug binding evasion, drug efflux, or enhanced activation of alternative signaling pathways are major factors that affect tumor fitness[2-5]. Defining the role of growth cues within the tumor microenvironment remains a growing area of investigation[6-8].

Basal cell carcinoma (BCC) of the skin is the most common human cancer and provides an ideal system to study tumor evolution. BCCs invariably result from mutations in hedgehog receptors Patched (PTCH1) or Smoothened (SMO), causing constitutive hedgehog (HH) pathway activation. Vismodegib, a targeted agent against SMO, recently received FDA approval for the treatment of advanced BCCs. Unfortunately, fewer than 50% of patients with advanced or metastatic BCCs respond at the time of treatment with an additional 20% acquiring secondary resistance during the first year of treatment[9-11]. Similar to sporadic drug-naïve BCCs, patient resistant clones uniformly maintain activation of HH target genes[12], highlighting an undiminished dependence on the HH pathway for resistant growth.

Mutations in canonical hedgehog pathway genes that cause maintenance of GLI transcription factor activity in vismodegib-resistant BCCs have recently been uncovered at or downstream of SMO. Included are mutations generating constitutively active SMO, loss of hedgehog inhibitor suppressor of fused (*SUFU*), amplification of *GLI2* and *CCND1*, and activation of the polarity kinase *aPKC*[12-14]. Despite our sequencing efforts, approximately 50% of patient resistant BCCs contained no detectable HH pathway variants and the majority of *SMO* variants identified were non-functional, despite maintaining elevated HH activation[12,15]. These data strongly support the existence of one or more unidentified non-canonical resistance pathways.

Here, we use a new murine model of BCC resistance and patient-derived tumors, along with multi-dimensional genomics, to identify a key role for the transcription factor, serum response factor (SRF). SRF was previously reported to drive two competing, mutually exclusive transcriptional programs by associating with transcriptional cofactors ELK1 and megakaryoblastic leukemia 1/2 (MKL1/2, also known as MRTF-A/B and MAL)[16-20]. In the latter pathway, RhoA-dependent signal inputs promote actin polymerizing proteins Rho-associated protein kinase (ROCK) and formin family member Diaphanous (mDia), causing restructuring of G-actin to F-actin. This restructuring liberates cytoplasmic MKL1, allowing this transcription factor to move into the nucleus to activate MKL-dependent gene expression. We define the MKL1/SRF cytoskeletal signaling pathway as a non-classical component of the HH pathway that amplifies downstream HH activation and drug resistant tumor growth. Additionally, we show MKL1 inhibitors have considerable efficacy in treating resistant BCCs *in vivo*, implicating the cytoskeletal-sensing SRF/MKL1 pathway as a promising new therapeutic target for resistant BCCs.

RESULTS

PTC53 mice mimic human drug resistant BCC phenotypes

While previous analysis of the mutational landscape of patient-derived resistant BCCs uncovered variants in the canonical HH pathway[12,13], less than half contained canonical mutations, many of which were non-functional[15]. This revealed the existence of one or more unknown yet prevalent non-canonical resistance pathways in human BCCs. To identify and characterize these non-canonical pathways, we interrogated a new mouse tumor resistance model that more closely resembled the clinical scenario in patient BCCs. We utilized Ptch1+/-, K14-Cre-ER, p53 fl/fl (PTC53-BCC) mice which were previously reported to develop primary tumors resembling human BCCs after a single dose of radiation[21]. Drug naive tumors were passaged into NOD/SCID recipients and intermittently treated with the SMO inhibitor GDC-619 over several cycles spanning a 3-month period (Fig. 1a-b and Supplementary Fig. 1a, 1f). Remarkably, intermittent SMO inhibition resulted in progressive generation of both sensitive (sBCC) and resistant BCCs (rBCC) that resembled human BCCs by histology and BCC marker expression (Fig. 1c-g). In the presence of SMO inhibitor, sensitive and resistant BCCs were defined as those with a net regression or active growth, respectively (Supplementary Fig. 1b). Like human BCCs, nodular, morpheic, and Pinkus subtypes were represented, arguing that these histological subtypes do not correlate with SMO inhibitor resistance behavior (Fig. 1c and data not shown).

To characterize our mouse tumors further, we identified expression changes using whole transcriptome analysis by RNA sequencing (RNA-seq). Differential expression analysis comparing resistant versus sensitive mouse tumors uncovered significantly up or down-regulated mRNAs in resistant BCCs (Fig. 1d). Similar to human rBCCs, each of the resistant mouse BCCs expressed high levels of *GLI1* and *PTCH1* at both the mRNA and protein levels (Fig. 1e-g), indicative of HH pathway activation. These tumors lacked markers of other keratinocyte-derived tumors such as immunoreactivity to the MAP kinase pathway marker, phospho-ERK (Supplementary Fig. 1c-d). Additional BCC markers (EPCAM, BCL2, GLI2, and ACTA2) were expressed at high levels relative to squamous cell carcinoma markers Involucrin (IVL), SOX2, and CDKN2A (Supplementary Fig. 1e). Thus, we conclude that the PTC53-BCC mouse line is a novel source of clinically-relevant rBCCs.

Multi-dimensional genomics uncovers activated SRF in resistant human and mouse BCCs

To identify non-canonical tumor escape mechanisms that maintain elevated HH signaling, we reasoned that non-canonical transcription factors (TFs) provide compensatory growth signaling through the GLI transcription factors downstream of SMO. To uncover potential cofactors, we screened for TFs co-occupying sites near GLI1 using the recently developed Feature Overlapper for Chromosomal Interval Subsets (FOCIS) algorithm[22]. This method compares input genomic coordinate data to a large dataset of genomic binding information from numerous datasets. Our input dataset consisted of FLAG-GLI1 genomic binding data from a HH-dependent medulloblastoma model, the only tumor-derived GLI chromatin immunoprecipitation sequencing (ChIP-seq) available at the time (see methods). Using FOCIS, we ranked TFs with chromosomal occupancy profiles enriched at GLI1 target genes and found 109 TFs with overlapping binding signatures (Fig 2a). Next, we utilized our

RNA-seq to identify TFs with enhanced activation in resistant BCCs using the Gene Set Enrichment Analysis (GSEA) TRANSFAC database. GSEA revealed 305 enriched target gene expression profiles in resistant versus sensitive tumors and highlighted selective activation of a subset of transcription factors (Fig 2b). To define putative TFs that are both enriched at HH target genes and selectively activated in resistant BCCs, we carried out multicomponent analysis that ranked TFs scoring high in both GSEA and FOCIS enrichment analyses. Of the possible 615 TFs, our multicomponent analysis identified serum response factor (SRF) as the top candidate resulting from numerous high confidence hits as a putative cofactor for GLI1 with increased transcriptional activity in resistant BCCs (Fig. 2c-d). Other TFs that scored highly in overlapping binding sites (Fig 2a) or with targets genes enriched in BCCs (Fig 2b), included hepatocyte nuclear factor-4, Ras-responsive element-binding protein 1, and ETS translocation variant. However, SRF represented the only TF expressed in BCCs with significant enrichment in both categories, focusing our effort on SRF as a strong candidate driver of BCC resistance.

To determine SRF's significance in human BCCs, we examined SRF activation using our human BCC transcriptome datasets[12]. GSEA analysis revealed similar SRF enrichment in both mouse and human rBCCs (Fig. 2d-e), and multi-component analysis also revealed significant SRF enrichment at GLI1 targets in human rBCCs (Fig 2f). We divided individual patient samples into those with known activating HH resistance mutations and those without canonical resistance variants. In samples with high allele frequency of classical HH pathway mutations, no SRF target gene enrichment was observed. However, in 3 of 4 tumors without a detectable canonical mutation, we observed positive SRF target gene enrichment (Fig. 2g), suggesting SRF activation is the predominant alternative pathway driving BCC resistance in non-*SMO* mutated tumors. Consistent with this observation, SRF target gene enrichment arose in resistant mouse tumors exhibiting negligible changes in SNV rate (Supplementary Fig. 2a). Similar to the 50% of human resistant tumors lacking SMO mutations[9,12,15], mouse PTC53-derived resistant BCCs contained low frequencies of SMO variants (Supplementary Fig. 2b). Intriguingly, additional FOCIS analysis revealed SRF enrichment at GLI1 target sites using ChIP-seq data from medulloblastoma (Fig. 2a-c), but not at GLI1 occupancy sites in the developing central nervous system or at GLI3 sites during limb bud formation (Supplementary Fig. 2c), indicating SRF binds to GLI sites in tumorigenic, but not developing tissues. Pathway enrichment terms from human and mouse RNA-seq data comparing transcriptome signatures for resistant versus sensitive BCCs (Supplementary Fig. 2d-e) suggest activation of cytoskeletal signaling networks[23]. Thus, we conclude that increased SRF transcriptional activity at GLI target genes correlates specifically with tumor resistance.

SRF and MKL1 are required for rBCC growth and elevated HH pathway activity

Our bioinformatic analyses suggest that SRF functions to induce GLI1 activity through proximal binding to DNA (Fig. 2a). To determine if GLI1 forms a complex with SRF, we carried out inverse Co-IP experiments using FLAG-tagged GLI1 and HA-tagged SRF. Indeed, antibodies to FLAG-tagged GLI1 pulled down HA-SRF, and IP using HA resin pulled down HA-SRF and FLAG GLI1 (Fig. 2h). Proximity Ligation Analysis (PLA) using two independent SRF antibodies highlights a SRF/GLI complex in situ (Supplementary Fig.

3-4). We next interrogated the role of SRF in rBCC growth. Using murine SMO inhibitor-resistant BCC cell lines (Supplementary Fig. 5a-b), knockdown of SRF expression caused a significant decrease in rBCC cell growth (Fig. 3a and Supplementary Fig. 5c-e) and downstream HH pathway output, measured by a decrease in *GLI1* mRNA expression (Fig. 3b). Taken together, our data indicates that SRF maintains downstream HH activity and is necessary for rBCC growth.

SRF transduces a wide variety of environmental cues and is known to act downstream of p38 MAP kinase, MAP kinase kinase (MEK), protein kinase A (PKA), and MKL1[24-27] to form distinct heterodimeric transcriptional complexes (Fig. 3c). To determine which of the upstream signals were required for SRF-driven BCC growth, we screened a panel of inhibitors in two distinct SMO inhibitor resistant cell lines for those that could inhibit cell growth and *GLI1* expression. Interestingly, only the MKL1 inhibitor, CCG-1423, possessed activity (Fig. 3d-f and Supplementary Fig. 5i, 5l, 5r-s), while inhibitors against other SRF-activating pathways (PKA, MEK-ERK, and p38) demonstrated little effect even at doses well above their IC50 (Supplementary Fig. 5f-n), supporting the specificity of MKL inhibition. Direct knockdown of MKL and treatment with two structurally distinct MKL1 inhibitors, CCG-203971 and CCG-100602 gave similar results (Supplementary Fig. 5t-v, 6). Human resistant BCCs responded to MKL inhibition with a similarly potent response rate (Fig. 3f, and Supplementary Fig. 7). To assess general toxicity, we measured cell viability of non-malignant epithelial cells treated with MKL1 inhibitors where we observed little response (Supplementary Fig. 5o-q), highlighting the tumor-specific nature of the signaling pathway. Finally, we used inverse pull downs in rabbit reticulocyte lysates to test whether MKL1 formed a complex with GLI1 and SRF (Fig. 2i). We found that GLI1 and SRF were immunoprecipitated with Myc-tagged MKL1, supporting our conclusion that GLI1 forms a previously unknown complex with SRF and MKL1.

We next asked whether activation of MKL1 was sufficient to activate HH target genes in non-malignant cells. MKL1 is kept inactive in the cytoplasm by binding to monomeric G-actin via its N-terminal RPEL domain[28] and deletion of the RPEL domain results in nuclear accumulation[20]. Expression of constitutively active MKL1 (MKL1-N*) in NIH-3T3 cells caused potentiation of HH pathway activity with sub-threshold SMO agonist (SAG) treatment while full-length MKL1 (MKL1-FL) had minimal activity in wild type cells (Fig. 3g and Supplementary Fig. 5w). This data suggests upstream activation of MKL1 is required to potentiate HH target genes and highlights a requirement for low-level hedgehog activation to be present. Thus, we conclude MKL1/SRF amplify the HH pathway by potentiating *GLI1*.

SRF-GLI1 occupy and regulate a distinct subset of target genes

To define the transcriptome-wide gene regulatory signature for MKL1 and SMO in rBCC cells, we carried out RNA-seq in rBCC cells treated with MKL1 and SMO inhibitors. RNA-seq analyses indicated that 1448 genes are dependent on MKL1 and only 139 genes required SMO for expression, with 50 genes overlapping between datasets (Fig. 3h-i). To further investigate the gene regulatory mechanism for SRF and GLI1, we identified genomic regions directly occupied by SRF and GLI1 using chromatin immunoprecipitation (ChIP) followed

by sequencing (ChIP-seq). We identified 6519 ChIP peaks for SRF and 4638 peaks for GLI1 with 632 sites overlapping (Fig. 3j). Consistent with our FOCIS analyses (Fig. 2a-c), GLI1 occupied binding sites in close proximity to SRF ChIP peaks (Fig. 3k-l). ChIP peak profiles indicated that SRF occupancy in the 5'UTR of HH pathway activators *GLI1* and *GLI2* but not HH repressors *GLI3* and *PTCH1* (Fig. 3m and Supplementary Fig. 8a-c), suggesting SRF/MKL1 amplify HH activity by regulating expression of HH pathway activators.

Our multi-dimensional screen (Fig. 2) suggests that SRF binds to GLI1 target sites that are enriched in resistant BCCs, leading us to investigate whether SRF binding to HH targets required MKL1 and/or GLI1. We performed SRF and MKL1 ChIP qPCR to determine state-dependent SRF/MKL1 occupancy at GLI1/SRF co-bound HH target genes. Treatment with MKL1 inhibitor (CCG-1423) abolished the MKL1/SRF ChIP signal at these sites (Fig. 3n and Supplementary Fig. 9), indicating that MKL1 activation is required for occupancy. Interestingly, GLI1 inhibition with the aPKC inhibitor PSI, previously shown to prevent GLI1 association with chromatin[14], abolished SRF/MKL1 occupancy at HH target gene loci, suggesting GLI1 is also required for SRF/MKL1 recruitment to HH target genes. By contrast, SRF sites with no associated GLI1 ChIP signal (eg. FoxF1) did not require MKL1 or GLI1 for occupancy (Fig. 3n). Using RNA-seq data from resistant BCC cells (Fig. 3h-i) we determined if SRF-GLI1 co-bound genes required MKL1 for expression and found that *GLI1*, *CCND2* and *ACTB*, but not *GLI2*, required MKL1 for expression (Fig. 3o-r), showing MKL1 drives expression of a wide array of HH target genes in rBCC cells. Taken together, our results suggest GLI1 recruits SRF and MKL1 to HH target gene loci and the SRF/MKL1 complex is required to maintain elevated expression of HH target genes.

Nuclear MKL1 is present in the majority of resistant BCC

Nuclear SRF/MKL1 activity requires release of G-actin mediated inhibition of MKL1 in the cytoplasm[20,28]. Our bioinformatic analyses implicated SRF/MKL1 activation in rBCCs with little change in SRF or MKL1 expression levels (Supplementary Fig. 10), leading us to investigate the nuclear accumulation of MKL1 in human and mouse BCC samples. Biochemical and immunohistological subcellular localization studies demonstrated the presence of nuclear MKL1 in rBCC, but not in sBCC in mouse (Fig. 4a, c-d, n=16 for resistant and n=14 for sensitive) and human BCCs (Fig 4b, 4f-g, n=24 for resistant and n=11 for sensitive). Our human BCC data suggests tumors with constitutively active SMO (canonical resistance) do not require MKL1 activation for growth (Fig. 2g). To explore this idea further, we examined MKL1 compartmentalization in a mouse model of BCC resistance driven by the SMOM2 mutation and, consistent with our genomic data, found that MKL1 remains uniformly cytoplasmic when SMO is constitutively active (Supplementary Fig. 11). Subcellular fractionation using a rBCC cell line indicated both SRF and MKL1 are abundantly present in the nucleus (Fig. 4e). Taken together, our data supports the model that SRF and MKL1 become activated in rBCCs by upstream signals promoting nuclear accumulation of MKL1.

Actin cytoskeletal regulators are activated in resistant tumors and required for BCC cell growth

Our observation that SRF/MKL1 nuclear localization potentiates GLI-driven BCCs suggests local tumor stimuli provide the necessary activation to drive resistance. Previous studies demonstrated that Rho activation is the primary driver of G-actin incorporation into actin filaments (F-actin)[29]. Incorporation of F-actin causes a local reduction in G-actin availability resulting in decreased actin binding to the RPEL domain of MKL1. Release of G-actin binding causes MKL1 transport to the nucleus[30], leading us to examine the status of the Rho/actin pathway in rBCCs. Using a state-dependent antibody against activated Rho (Rho-GTP, Supplementary Fig. 12), we found that RhoA has increased activity in resistant compared to sensitive tumors (Fig. 5a-b and Supplementary Fig. 13). Further implicating RhoA, rBCC cells displayed sensitivity to sub-IC50 concentrations of Rho inhibitor treatment (Fig. 5c).

Active RhoA affects cytoskeletal changes through multiple mechanisms, including activation of Rho-associated protein kinase (ROCK) that stabilizes cofilin-mediated filaments, or through binding and autoinhibitory release of the diaphanous-related formin family member (mDia)[31,32]. We interrogated the necessity of these individual Rho effectors in our rBCC cell line through the use of specific inhibitors. ROCK inhibitors (Thiazovivin and Y27632) failed to suppress resistant BCC cell growth (Fig. 5d-e), however, mDia inhibition (SMIFH2) potently blocked BCC cell growth (Fig. 5f). To determine if actin cytoskeletal mediators were sufficient to potentiate GLI1 activity, we expressed Rho and mDia in NIH3T3 cells where we observed increased phalloidin staining, indicating increased F-actin (Supplementary Fig. 14a-e). We reasoned F-actin accumulation would result in MKL1 activation, thereby causing HH pathway activation. Indeed, Rho/mDia expression resulted in elevated *GLI1* expression with SAG stimulation (Fig. 5g), suggesting that cytoskeletal activation is sufficient to potentiate the HH pathway. This effect was abrogated by the MKL1 inhibitor CCG-1423, indicating that Rho and mDia act upstream of MKL1/SRF. Taken together, our data provides novel mechanistic details for a link between cytoskeletal regulators and HH pathway activation.

In vivo mouse and patient BCCs respond to MKL1 inhibitors

Our patient tissue and *in vitro* data suggest resistant tumors have evolved to activate a RhoA/mDia/actin/SRF/MKL1 pathway to potentiate GLI-dependent signaling and BCC growth. To determine therapeutic potential, we interrogated allografts of rBCCs generated from PTC53-BCC mice (Fig. 1) after treatment with the MKL1 inhibitor, CCG-203971 which has recently been shown to have *in vivo* tolerability[33,34]. Consistent with our *in vitro* growth data, systemic MKL1 inhibition caused a dramatic decline in resistant tumor growth *in vivo* compared to SMO inhibition in two independent parental tumor lines (Fig. 6a-b, and Supplementary Fig. 15). MKL1 inhibitors caused significantly reduced levels of *GLI1* expression (Fig. 6c), reflecting the dependence of our mouse resistant tumors on the HH pathway. SMO inhibition also caused a reduction in *GLI1* expression, however, *GLI1* depletion did not reach the threshold necessary for disease response (Fig. 6c) which is consistent with reports of moderate *GLI1* inhibition accompanying limited response in rBCC patients treated with arsenic trioxide and itraconazole[35]. MKL1 inhibitor, but not

vismodegib, prevented MKL1 recruitment into the nucleus of tumor cells and caused a reduction in proliferation index (Fig. 6d-e and Supplementary Fig. 16). Since sBCCs contain mainly cytoplasmic MKL, we predicted that sensitive BCCs and cell lines would respond to SMO inhibition but not MKL1 inhibitors. Indeed, sBCCs responded to SMO inhibitors but only weakly to CCG-203971 (Fig. 6f and Supplementary Fig. 17), suggesting MKL1 dependence predominates in SMO inhibitor-refractory tumors. Thus we conclude that systemic treatment with MKL1 inhibitors significantly improves tumor outcome compared to SMO inhibitors in resistant BCCs.

To determine the therapeutic potential of MKL1 inhibitors in advanced human BCCs and because of the inability to generate patient-derived xonografts (PDXs), we developed tumor explant culture conditions for 10 consecutive freshly resected patient advanced BCCs. In contrast to simple BCCs, advanced BCCs are naïve to SMO inhibitors but regularly exhibit partial SMO inhibitor resistance at the time of treatment[10,36]. We measured *GLI1* transcript levels in RNA extracts from tumor explants containing nuclear MKL1 where we observed a significant reduction in *GLI1* expression (Fig.6g-h and Supplementary Fig. 18) suggesting MKL1 inhibition may provide therapeutic benefit in this subset of patients. Similar to the naïve mouse tumors, patient tumors containing inactive cytoplasmic MKL1 did not respond to CCG-1423 (Fig. 6i-j and Supplementary Fig. 18g-l) indicating MKL1 inhibition has limited therapeutic benefit. Notably, treatment with the SMO inhibitor vismodegib produced a robust *GLI1* response in two independent tumors with cytoplasmic MKL1 (Fig. 6j and Supplementary Fig. 18i and l). Further quantification of MKL1 compartmentalization revealed a strong correlation between MKL1 nuclear accumulation and the response to MKL1 inhibitors in patient tumor explants (Fig. 6k). We conclude that MKL1 inhibition has in vivo efficacy in mouse rBCCs and human patient tumor explants. Our results uncover a novel mechanism by which the Rho kinase/MKL1/SRF pathway activates GLI1 activity causing resistance and demonstrate that inhibitors of the pathway provide a promising therapeutic avenue for patients with rBCCs.

DISCUSSION

Our tumor sequencing and histologic studies in our human patient samples highlight SRF/MKL1 activation as a dominant driver in the majority of resistant BCCs and validates our initial studies uncovered from our murine model of resistance. We reveal that the MKL1/SRF pathway acts as a novel parallel pathway to activate downstream hedgehog pathway activity by potentiating GLI1 transcriptional activity. Additionally, our studies demonstrated anti-tumor activity for MKL1 inhibitors in both patient tumor explants and our mouse model of resistance providing preclinical justification to add MKL1 as a novel therapeutic target to the cancer armamentarium.

We demonstrated that nuclear MKL1 is predominant in the majority of resistant BCCs (Fig. 4) highlighting this resistance mechanism as a dominant driver of tumor resistance. It should be noted that tumor burden was reduced in sensitive mouse tumors treated with MKL1 inhibitor (p<0.05), however, the effect was much more pronounced with SMO inhibitor treatment in these naïve tumors (Fig. 6f). This suggests a small amount of tumor heterogeneity in drug-naïve mouse tumors. In fact, 6 out of 10 highly advanced human naïve

BCCs displayed high levels of nuclear MKL1 (Fig. 6k), suggesting this pathway plays a major role in innate BCC resistance which is present in ~60% of advanced drug-naïve BCCs[36]. We knocked-down expression of addition RPEL proteins (Phactr1 and KDM3A) and observed no change in HH pathway activity (Supplementary Fig. 19), suggesting MKL is unique among RPEL proteins with respect to HH pathway modulation. Our GSEA analyses indicate SRF is activated only in patient tumors that do not contain SMO mutations (Fig. 2g). Notably, we demonstrate that this "nuclear MKL1 patient group" responds favorably to MKL1 inhibitors by reducing *GLI1* expression (Fig. 6k). Our initial study demonstrated predominantly cytoplasmic MKL1 in sporadic human BCCs with a few small regions containing nuclear MKL1 (Fig. 4f and data not shown). However, nuclear MKL1 appears to be enriched in highly advanced human naïve BCCs (Fig. 6k) and enriched further in cases resistant to SMO inhibitors (Fig. 4g). Thus, tumor heterogeneity with respect to MKL1 nuclear localization underpins the need to define patient subtype to inform us of therapeutic outcome.

Our observation that GLI1 binds near but not directly at the center of the SRF enrichment profile suggests these TFs may exist as part of a large TF complex. Consistent with this hypothesis, GLI1, SRF, and MKL1 form a complex (Fig. 2h-i), however, GLI1 and SRF chromatin binding do not overlap directly, suggesting they interact on DNA (Fig. 3l and Supplementary Fig. 20). Additionally, GLI1 directs SRF occupancy at GLI-bound target sites (Fig. 3n), which is consistent with previous work indicating SRF target specificity is determined by its binding partners[17,19]. We did not observe a change in MKL1 compartmentalization upon Gli1 inhibition (Supplementary Fig. 21) suggesting Gli1 recruits MKL through an intranuclear mechanism. We detected PLA signal using GLI1 and SRF antibodies (Supplementary Fig. 3-4), however, we did not observe PLA signal for GLI1 and MKL1 (data not shown). This observation suggests closer proximity for GLI1-SRF relative to GLI1-MKL, however, both SRF and MKL1 exist in a complex with GLI1 (Fig. 2h-i). GLI1 target binding identified in this study (Fig. 3m-n) was not observed in previous SRF and MKL1 ChIP-seq datasets[37,38]. However, ENCODE datasets do contain SRF ChIP signals at both HH targets and other oncogenic promoters in tumor, but not normal tissues (Supplementary Fig. 22), illustrating how SRF recruitment by GLI1 further broadens its genomic binding capabilities in the context of tumor resistance. The necessity for GLI1 recruitment comes from the finding that Rho/mDIA/SRF/MKL1 activity is not sufficient to induce *GLI1* (Fig. 3g and 5g), and SRF/MKL1 does not activate other TF pathways tested in BCCs (data not shown). A recent report highlighted an interaction between MKL1 and JMJD1A that destabilized GLI1 at the protein level and caused suppression of HH pathway activation[39]. However, JMJD1A is not expressed in human or mouse BCCs, indicating rBCCs have evaded this GLI1 protein stabilization mechanism.

Our study provides a strong physiological connection between tumorigenic HH signaling and SRF/MKL1 that has not been explored previously. Emerging studies on the role of HH signaling in the fibrotic response of scleroderma[40] along with the established role of SRF-MKL1 in inflammation suggest that rBCCs, although expressing canonical keratinocyte markers, have acquired characteristics of myofibroblasts. Previous studies have attributed cytoskeletal alteration in tumor progression to the increased mobility and deformability of activated cells[41]. Moreover, Rho activation is known to increase metastatic ability through

the actin cytoskeleton and indirectly through SRF/MKL1 activation[20,42]. Our human and mouse RNA-seq data highlights an upregulation of genes involved in integrin activation (Supplementary Fig. 2d-e), a known activation pathway upstream of Rho. Our data is consistent with a recent finding that compares human BCCs to normal skin, uncovering integrin activation as the most highly enriched pathway term[23]. This suggests many sporadic human BCCs have upregulated adhesion signaling which may play a role in the 50-70% of patients who develop resistance[36]. The source of integrin activation likely results from changes within the extracellular matrix suggesting that the tumor microenvironment plays an important role in resistant growth. The observation that BCCs do not grow in patient-derived xenografts further suggests a role for the tumor stroma in BCC viability. In our study, we addressed this by developing culture conditions for patient derived explants (Fig. 6 g-k). Efforts to improve culture conditions to facilitate additional assays (e.g. growth assays) are ongoing. Our finding that mDia, but not ROCK, is required downstream of Rho for rBCC growth (Fig. 5d-f), adds an additional mechanistic detail and potential therapeutic target to treat SMO inhibitor-refractory patients. A previous study describes an inhibitory role for mDia1 on DYRK1A-dependent GLI transcription[43]. We find that mDia promotes GLI-dependent transcription (Fig. 5g), suggesting DYRK1A and Rho stimulate mDia to cause opposing outcomes on the HH pathway. How mDia promotes these opposing outcomes is an important area for future investigation. Taken together, our work suggests the tumor microenvironment provides pro-growth signaling to promote cytoskeletal remodeling and resistance to targeted therapies by potentiating GLI signaling (Supplementary Fig. 23).

This study adds a potent and exciting therapeutic target for future cancer treatment. Our multicomponent genomic analyses highlight SRF/MKL1 as novel activators of HH-dependent transcription and we utilize this finding to target MKL1 with pharmacological inhibitors to treat rBCCs. Our *in vivo* mouse (Fig. 6a-f) and patient tumor explant (Fig. 6g-k) data highlight the therapeutic potential of MKL1 inhibitors in human BCCs. Previous studies have focused on the role of SRF/MKL1 in inflammation[44], however, our work provides pre-clinical justification to extend MKL1 inhibitors to oncogenic therapy. The demonstration that SRF/MKL1 can potentiate oncogenic driver pathways opens the possibility of using MKL1 inhibitors in other tumor types. The use of MKL1 inhibitors in conjunction with SMO inhibitors is likely to synergize given the parallel nature of these signaling pathways in BCCs, thus, combination therapy will be a major focus as these inhibitors move toward clinical development.

METHODS

Patient case samples

Written informed consent was obtained for all human subject samples and reviewed by Stanford University Institutional Review Board. Resistant and sensitive BCCs were defined using the Response Evaluation Criteria in Solid Tumors (RECIST) method. Progressive or stable growth of BCC tumors with continuous treatment with vismodegib (150mg per day) were defined as resistant tumors. BCCs exhibiting partial or complete regression with vismodegib treatment (150mg per day) were defined as sensitive tumors as defined by RECIST.

Ptch +/-, K14-Cre-ER, p53 fl/fl Mice

All mice were housed under standard conditions and animal care was in compliance with the protocols approved by the Institutional Animal Care and Use Committee (IACUC) at Children's Hospital Oakland Research Institute (CHORI) and Stanford University (#11680). Ptch1+/-K14-Cre-ER2 p53fl/fl (BCC) mice were generated passaged and utilized to develop BCC tumors as described previously [45,46]. Here we irradiated mice (5Gy) using an X-ray irradiator. For in vivo validation of MKL1 inhibition, resistant tumors were passaged into NOD/SCID mice using the method outlined above. Mice received drug treatment by i.p. injection daily for 15 days using 100 mg/kg for CCG203971 (Cayman Chemical) and vismodegib (Selleckchem). Treatment was administered starting at the time of tumor passage for both CCG203971 and vismodegib. For initial resistant tumor generation and drug treatment in drug-naïve BCCs (Fig. 6f), the Smo inhibitor XL-139 was administered by oral gavage every 48 hours (25mg/kg) to NOD/SCID mice containing BCC allografts.

Mouse whole exome tumor sequencing

Whole exome sequencing (exome-seq) of mouse tumors was carried out using tissue frozen in RNA later (Ambion) at -80 °C. DNA was isolated using the DNeasy Blood & Tissue Kit (Qiagen). Exome capture was carried out with 2ug of DNA using the Agilent SureSelectXT kit. Sequencing to generate paired-end100bp reads were obtained using isolated whole exomes sequenced on the Illumina HiSeq 2500 platform. Our exome-seq pipeline produced a mean coverage of 195X within coding regions. Sequencing reads were aligned to the mouse reference genome sequence (mm9) using BWA. SAM to BAM conversion was carried out using Picard tools, and local realignment around indels with base quality score recalibration was performed using the Genome Analysis Toolkit (GATK). Single nucleotide variants (SNVs) were called using (GATK). The annotation of non-synonymous SNVs was performed using Annovar. Comparison to human BCC mutational landscape was performed using previously published variants [47]. *Smo* mutation was identified by calling variants on unfiltered alignment files using Samtools and annotated using snpEff using the GRCm38.71 genome.

RNA sequencing and bioinformatic screening

Library preparation, sequencing and mapping were carried out as described previously [47] with minor modifications. Alignment was carried out with TopHat using mm9 as a reference genome. DEseq was used to create a pre-ranked gene list of genes differentially expressed in resistant versus sensitive tumors, and this list was used to perform gene set enrichment analysis (GSEA, Broad Institute) using the TRANSFAC database for transcription factor targets. Enriched transcription factors were ranked by false discovery rate (FDR) from GSEA analysis, which is presented in Figure 2. Additional GSEA analysis was carried out using RNA-seq data from published human patient resistant (n = 6) and sensitive (n = 4) BCCs [47] which were ranked by FDR score as described above. Pathway enrichment terms from RNA-seq data was obtained using Enrichr[48].

GLI1 ChIP-seq data was obtained from mouse embryonic central nervous system[49], mouse granular neural progenitors (GNPs) (Supplementary Data Fig. 2c) and medulloblastoma (Fig. 2a, 2c) (Brown et al. *submitted*), and an additional dataset of mouse GNPs[50]. GLI3

ChIP-seq data was obtained from mouse embryonic limb bud [51]. These data are available using GEO accession codes GSE42132, GSE42594, GSE17682, and GSE11062.

Transcription factors sharing occupancy sites with GLI1 and GLI3 were identified using the feature overlapper for chromosomal interval subsets (FOCIS) as described previously [52]. FOCIS pattern matches transcription factor binding signatures from chromosomal interval data (GLI1 ChIP-seq in our case) with the curated datasets for ENCODE, TRANSFAC, JASPER, Swiss Regulon, HOCOMOCO, and UCSC Conserved TFBS databases. To determine enrichment at GLI1 or GLI3 binding sites, subset and background datasets were generated using GLI1 or GLI3 ChIP-seq data (accession codes indicated below). Putative GLI1 cofactors were ranked by FOCIS enrichment (z-score). Enrichment scores were generated by converting z-scores to a scale between 0 and -/+1. Multi-dimensional genomic analysis was performed by plotting GSEA rank and FOCIS enrichment along the x and y axes respectively (Fig. 2c). Additional multi-dimensional analyses was carried out using GSEA data from human RNA-seq read values as described above. GSEA enrichment scores for SRF were obtained for individual human resistant tumors by running the GSEA algorithm for each resistant tumor compared to the mean sequencing values for all sensitive tumors in the dataset. Human whole exome-seq and RNA-seq datasets are publically available using GEO accession numbers GSE58374, GSE58375, GSE58376, and GSE58377. Mouse RNA-seq and whole exome sequencing generated in this manuscript are available using GEO identifier GSE78497.

Chromatin immunoprecipitation

ASZ001 cells were used to isolate protein DNA complexes to map chromatin occupancy for endogenous SRF was carried out as described previously [50] with minor modifications. Cells were crosslinked with 1% formaldehyde for 10min. Cells were lysed in modified RIPA buffer (50mM Tris, 150mM NaCl2, 1% Triton X100, 0.75% SDS, 0.5% Sodium Deoxycholate), which was supplemented with protease and phosphatase inhibitor cocktail (Roche). Cellular extracts were sonicated using a Covaris B208 ultrasonicator to produce chromatin fragments between 100 to 400bp. Cleared extract was incubated with 5ug of antibody against SRF (Santa Cruz), or non-specific IgG control antibody (Cell Signaling) overnight and precipitated using protein A/G sepharose beads. Beads were washed with ChIP wash buffer (100mM Tris pH 9.0, 500mM LiCl, 1% Igepal, 1% Deoxycholic Acid, protease inhibitor cocktail [Roche]) and protein/DNA complexes were eluted with IP elution buffer (1%SDS, 50mM NaCOH$_3$). Crosslinks were reversed by incubation at 67°C overnight while shaking at 1400rpm on a thermoshaker. RNA was digested with 0.2ug/ml RNase A at 37°C for 30 min. DNA was isolated using Qiagen min elute columns using manufacturers instructions. Relative fold enrichment of SRF was determined by adding DNA to Brilliant II SYBR Green qPCR Master Mix Kit (Agilent Technologies). ChIP with non-specific IgG control antibody incubated with ASZ001 extract was used as a control to calculate fold enrichment.

ChIP-seq libraries were generated using the standard protocol for the NEB-Illumina library preparation kit (New England BioLabs). ChIP libraries were sequenced using the Illumina HiSeq 4000 platform. Alignment was carried out with TopHat using mm9 as a reference

genome. High confidence peaks were obtained using MACS2 (p<0.0001). Background removal was carried out by submitting replicates to IDR filtering. DEseq used to determine enrichment at GLI1 and SRF peaks. Heatmap and histogram were generated using the annotatePeaks.pl script in Homer suite as described previously[53]. Heatmap data was visualized using Java TreeView. Read pileups at genomic loci were imaged using Integrated Genomics Viewer (Broad Institute). High confidence peaks were annotated for gene associations using the Genomic Regions Enrichment of Annotations Tool (GREAT)[54].

Immunofluorescence

BCC tumors were fixed with 4% paraformaldehyde and embedded in paraffin blocks. 5μm sections were mounted onto glass slides and stained with hematoxylin and eosin, or immunolabeled using antibodies listed below. Cells plated in 8-well chamber slides (Millipore) were fixed using 3.7% formaldehyde diluted in phosphate buffered saline for 10 minutes. Sections/chamber slides were immunostained using a previously described protocol (Cell Signaling Technologies general IF protocol) using indicated antibodies and dilutions: anti-SRF (1:100, Santa Cruz Biotechnology, sc-335) (Supplementary Fig. 24), anti-keratin 14 (1:500, Abcam, ab130102), GLI1 (1:100, R&D Systems, AF3455) (Supplementary Fig. 25), MKL1 (1:200, Sigma, HPA030782) (Supplementary Fig. 26), beta tubulin (1:500, DSHB, E7), Ki-67 (1:1000, Abcam, ab15580). Fluorescent-labeled secondary antibodies utilized: Alexa Fluor 488, Alexa Fluor 555, Alexa Fluor 594, and Alexa Fluor 647 (1:500, Life Technologies). Confocal imaging was carried out using a Leica SP8 microscope equipped with adjustable white light laser and hybrid detectors. To quantify *GLI1* expression in BCCs (Figure 1), pixel intensity measured using image J in regions staining positive for keratin 14. For each condition (sensitive and resistant) 3 fields were counted in 5 independent tumors for a total of 15 data fields per condition. Subcellular localization of SRF and MKL1 (Figure 2) was quantified using multi-position intensity profiles using the Image J multi-plot plug in. Keratin 14 and DAPI staining were utilized as guides to determine cytoplasmic and nuclear localization respectively. Percentage of cells staining positive for nuclear MKL1 in human patient BCCs was carried out by flash freezing tumor fragments and imbedding in OCT for cryosectioning. Nuclear MKL1 was counted using DAPI as a guide for nuclei and K14 as a guide for tumor area. Actin filament staining was carried out using phalloidin 488 and 647 (Life Technologies).

Proximity ligation assay (PLA) staining was carried out using co-labeling with primary antibodies against GLI1 (raised in goat) with SRF (raised in rabbit), GLI1 with MKL1 (raised in rabbit), and GLI1 with non-specific rabbit IgG (Cell Signaling). Secondary antibodies consisted of Duolink goat plus (Sigma, DUO92003) and rabbit minus (Sigma, DUO92005). Detection of complexes was carried out using Duolink Red in situ reagents (Sigma, DUO92008).

Immunoblotting

Whole cell extracts were harvested using radioimmunoprecipitation (RIPA) buffer supplemented with protease and phosphatase inhibitors (Roche) and run on SDS-PAGE gels (Life Technologies) then transferred onto nitrocellulose membranes. To prepare nuclear extracts, cells were resuspended in hypotonic lysis buffer (10mM HEPES, pH7.9, 1.5mM

MgCl$_2$, and 10mM KCl) and dounced 15 times. Isolated nuclei were pelleted and resuspended in RIPA buffer. Immunoblotting was carried out using antibodies against the following proteins: GLI1 (Cell Signaling) (Supplementary Fig. 27), beta-tubulin (Developmental Studies Hybridoma Bank), Flag M2 (Sigma), HA (Abcam) (Supplementary Fig. 28), GAPDH, Histone H3, SRF, MKL1 (Santa Cruz Biotechnology). All immunoblots imaged using the LI-COR Odyssey image system.

Cell Culture

ASZ001 and BSZ001 BCC cells were cultured in 154CF media (Life Technologies) supplemented with 2% chelated fetal bovine serum and 0.05mM CaCl$_2$. Experiments carried out using low serum conditions contained 154CF media containing 0.2% chelated FBS and 0.5nM CaCl$_2$. NIH-3T3, HaCaT, and HEK-293T cells were cultured in DMEM supplemented with 10% fetal bovine serum. Hedgehog induction experiments carried out using low-serum DMEM containing 0.5% FBS. UW-BCC1 cells (human BCC cells) were isolated from a patient with superficial BCC. Cells were cultured as described previously[55].

Co-Immunoprecepitation

Expression of N-terminal Flag-tagged GLI1 (Flag-GLI1) and HA-tagged SRF (HA-SRF) was carried out in HEK-293T cells using the pCS2 backbone. Transiently transfected cells were harvested from 80% confluent 10cm plates. Lysis buffer consisted of Tris buffered saline pH 7.4, 1% Triton X-100, and protease inhibitor cocktail (Sigma). Cleared lysates were incubated overnight with Flag M2 magnetic beads (Sigma), HA magnetic beads (Thermo Fisher), or IgG control beads (Thermo Fisher). Protein was eluted in 50ul RIPA buffer containing protease inhibitor cocktail. Additional pull down experiments were carried out using the TNT SP6 Quick Coupled Transcription/Translation System (Promega). Expression of Flag-GLI1, HA-SRF, and c-terminal Myc-tagged MKL1 (myc-MKL1) was carried out using the pCS2 backbone. Tagged MKL1 was pulled down using anti-c-myc magnetic beads (Thermo Fisher). Cell free extracts were eluted after pull down using 50ul of RIPA supplemented with protease inhibitor cocktail. All pull down extracts were immunoblotted using the method described above.

SRF knockdown and inhibitor treatment

Knockdown of SRF was achieved by lentiviral transduction using short hairpin RNAs expressed in the pLKO.1 backbone (Open Biosystems). Cell growth assays were performed by plating subconfluent ASZ001 and BSZ001 cells in 96-well plates in low serum media followed by addition of inhibitors or lentiviral shRNAs. MTS assays were carried out according to manufacturers instructions (Promega) 72 hours after transduction/inhibitor treatment. Expression of protein and RNA was measured in stably transduced cells within 3 passages or 24 hrs after inhibitor treatment. Transient knockdown for SRF, MKL, Phactr1, and KDM3A was achieved by transfection of ASZ001 cells with antisense siRNAs (Sigma-MISSION). Transfection of siRNAs was carried out using RNAiMAX transfection reagent (Thermo Fisher). Quantitative PCR (qPCR) was carried out to measure expression of SRF and hedgehog target, GLI1.

The following inhibitors were used to suppress activity of the signaling proteins indicated below: MKL1 (CCG-1423, CCG-203971, CCG-100602 – Cayman Chemical), Smoothened (Vismodegib – Selleckchem), MEK1/2 (PH797804 and UO126 – Selleckchem), p38 MAP kinase (SB239063 – Tocris Bioscience), RHO (RHO inhibitor 1 – Cytoskeleton Inc), RHO-Associated Protein Kinase (ROCK) (Thiazovivin, Y27632 – Selleckchem), and mDia (SMIFH2 – Sigma). The following small molecules were utilized to stimulate activity of adenylyl cyclase (Forskolin – Selleckchem), and Smoothened (SAG – Cayman Chemical).

Patient tumor explant culture and drug treatment

Freshly resected tumors were obtained from advanced BCC patients receiving Mohs surgery. Informed consent was obtained in writing for all patient samples and reviewed by Stanford University Institutional Review Board. Tumor subtype was verified by immediate histological examination of resected BCCs. Patient specimens were cultured in EpiLife media supplemented with 0.05mM $CaCl_2$. Pharmacological inhibitors (CCG-1423 and Vismodegib) were incubated with tumors specimens for 24 hours. Drug-treated tissues were suspended in RLT buffer (Qiagen) and homogenized using 2ml tissue lysing matrix E tubes (MP Biomedicals). RNA was isolated from tumors using the RNeasy standard protocol (Qiagen). RNA extracts used to carry out qPCR using Taqman probes for human GLI1 and GAPDH (Thermo Fisher). MKL1 localization was assessed in explant specimens by freezing samples in OCT reagents and sectioning blocks for immunofluorescence analysis.

Statistical analysis

Experimental data for in vitro assays were tested for statistical significance against indicated control using unpaired Students t-test. All in vitro assays were carried out in triplicate (n = 3) unless otherwise noted. For initial mouse RNA and exome sequencing, n = 4 for each group (sensitive and resistant). Statistically significant changes in expression for resistant versus sensitive was determined using the DESeq algorithm with a cutoff of P<0.05. Gene set enrichment analyses were analyzed using a false discovery rate (FDR) cutoff of 0.2 and P<0.05. Immunofluorescence (IF) staining profiles (Fig. 4c-d, f-g, and Supplementary Fig. 11) were analyzed for similarity compared to a cytoplasmic marker (K14) using Pearson correlation analysis. For IF analyses n = 16 for resistant and n = 14 for sensitive mouse tumors, and n = 24 for resistant and n = 11 for sensitive human tumors. For in vivo inhibitor studies in mice (Fig. 6a-b), biological replicates (n = 4) were used for each condition. For human patient explant inhibitor studies (Fig. 6g-k), 10 tumors were analyzed using four experimental technical replicates (n = 4) per data point shown in Fig. 6h, j, k, and Supplementary Fig. 18. No mouse or human tumors were excluded from our studies. Statistical significance for P values obtained in all figures is indicated. *P < 0.05, **P < 0.01, ***P < 0.001, and ns = "not significant" unless otherwise noted. All data are reported as mean ± SEM unless otherwise noted. A normal distribution was observed for all data.

DATA AVAILABILITY AND ACCESSION CODE AVAILABILITY

Human whole exome-seq and RNA-seq datasets from previous studies are publically available and can be found using GEO accession codes GSE58374, GSE58375, GSE58376,

and GSE58377. Sequencing data generated for the current study are available using GEO identifier GSE78497.

Supplementary Material

Refer to Web version on PubMed Central for supplementary material.

Acknowledgments

References

1. Junttila MR, de Sauvage FJ. Influence of tumour micro-environment heterogeneity on therapeutic response. Nature. 2013; 501:346–354. [PubMed: 24048067]

2. Ransohoff KJ, Tang JY, Sarin KY. Squamous Change in Basal-Cell Carcinoma with Drug Resistance. The New England journal of medicine. 2015; 373:1079–1082.

3. Atwood SX, Whitson RJ, Oro AE. Advanced treatment for basal cell carcinomas. Cold Spring Harbor perspectives in medicine. 2014; 4:a013581. [PubMed: 24985127]

4. Amaral L, et al. Inhibitors of bacterial efflux pumps that also inhibit efflux pumps of cancer cells. Anticancer research. 2012; 32:2947–2957. [PubMed: 22753759]

5. Thomas-Schoemann A, et al. Drug interactions with solid tumour-targeted therapies. Critical reviews in oncology/hematology. 2014; 89:179–196. [PubMed: 24041628]

6. Nurnberg A, Kitzing T, Grosse R. Nucleating actin for invasion. Nature reviews Cancer. 2011; 11:177–187. [PubMed: 21326322]

7. Barker HE, Paget JT, Khan AA, Harrington KJ. The tumour microenvironment after radiotherapy: mechanisms of resistance and recurrence. Nature reviews Cancer. 2015; 15:409–425. [PubMed: 26105538]

8. McMillin DW, Negri JM, Mitsiades CS. The role of tumour-stromal interactions in modifying drug response: challenges and opportunities. Nature reviews Drug discovery. 2013; 12:217–228. [PubMed: 23449307]

9. Basset-Seguin N, Sharpe HJ, de Sauvage FJ. Efficacy of Hedgehog Pathway Inhibitors in Basal Cell Carcinoma. Molecular cancer therapeutics. 2015; 14:633–641. [PubMed: 25585509]

10. Sekulic A, et al. Efficacy and safety of vismodegib in advanced basal-cell carcinoma. The New England journal of medicine. 2012; 366:2171–2179. [PubMed: 22670903]

11. Chang AL, Oro AE. Initial assessment of tumor regrowth after vismodegib in advanced Basal cell carcinoma. Archives of dermatology. 2012; 148:1324–1325. [PubMed: 22910979]

12. Atwood SX, et al. Smoothened variants explain the majority of drug resistance in Basal cell carcinoma. Cancer cell. 2015; 27:342–353. [PubMed: 25759020]

13. Sharpe HJ, et al. Genomic analysis of Smoothened inhibitor resistance in basal cell carcinoma. Cancer cell. 2015; 27:327–341. [PubMed: 25759019]

14. Atwood SX, Li M, Lee A, Tang JY, Oro AE. GLI activation by atypical protein kinase C iota/lambda regulates the growth of basal cell carcinomas. Nature. 2013; 494:484–488. [PubMed: 23446420]

15. Atwood SX, et al. Rolling the Genetic Dice: Neutral and Deleterious Smoothened Mutations in Drug-Resistant Basal Cell Carcinoma. The Journal of investigative dermatology. 2015

16. Zaromytidou AI, Miralles F, Treisman R. MAL and ternary complex factor use different mechanisms to contact a common surface on the serum response factor DNA-binding domain. Molecular and cellular biology. 2006; 26:4134–4148. [PubMed: 16705166]

17. Wang Z, et al. Myocardin and ternary complex factors compete for SRF to control Smooth muscle gene expression. Nature. 2004; 428:185–189. [PubMed: 15014501]

18. Marais R, Wynne J, Treisman R. The SRF accessory protein Elk-1 contains a growth factor-regulated transcriptional activation domain. Cell. 1993; 73:381–393. [PubMed: 8386592]

19. Janknecht R, Nordheim A. Elk-1 protein domains required for direct and SRF-assisted DNA-binding. Nucleic acids research. 1992; 20:3317–3324. [PubMed: 1630903]

20. Miralles F, Posern G, Zaromytidou AI, Treisman R. Actin dynamics control SRF activity by regulation of its coactivator MAL. Cell. 2003; 113:329–342. [PubMed: 12732141]

21. Wang GY, et al. Establishment of murine basal cell carcinoma allografts: a potential model for preclinical drug testing and for molecular analysis. The Journal of investigative dermatology. 2011; 131:2298–2305. [PubMed: 21833014]

22. Webster DE, et al. Enhancer-targeted genome editing selectively blocks innate resistance to oncokinase inhibition. Genome research. 2014; 24:751–760. [PubMed: 24443471]

23. Bonilla X, et al. Genomic analysis identifies new drivers and progression pathways in skin basal cell carcinoma. Nature genetics. 2016; 48:398–406. [PubMed: 26950094]

24. Olson EN, Nordheim A. Linking actin dynamics and gene transcription to drive cellular motile functions. Nature reviews. Molecular cell biology. 2010; 11:353–365. [PubMed: 20414257]

25. Heidenreich O, et al. MAPKAP kinase 2 phosphorylates serum response factor in vitro and in vivo. The Journal of biological chemistry. 1999; 274:14434–14443. [PubMed: 10318869]

26. Zhang HM, et al. Mitogen-induced recruitment of ERK and MSK to SRE promoter complexes by ternary complex factor Elk-1. Nucleic acids research. 2008; 36:2594–2607. [PubMed: 18334532]

27. Blaker AL, Taylor JM, Mack CP. PKA-dependent phosphorylation of serum response factor inhibits smooth muscle-specific gene expression. Arteriosclerosis, thrombosis, and vascular biology. 2009; 29:2153–2160.

28. Pawlowski R, Rajakyla EK, Vartiainen MK, Treisman R. An actin-regulated importin alpha/beta-dependent extended bipartite NLS directs nuclear import of MRTF-A. The EMBO journal. 2010; 29:3448–3458. [PubMed: 20818336]

29. Mokady D, Meiri D. RhoGTPases - A novel link between cytoskeleton organization and cisplatin resistance. Drug resistance updates : reviews and commentaries in antimicrobial and anticancer chemotherapy. 2015; 19:22–32. [PubMed: 25660168]

30. Guettler S, Vartiainen MK, Miralles F, Larijani B, Treisman R. RPEL motifs link the serum response factor cofactor MAL but not myocardin to Rho signaling via actin binding. Molecular and cellular biology. 2008; 28:732–742. [PubMed: 18025109]

31. Li F, Higgs HN. The mouse Formin mDia1 is a potent actin nucleation factor regulated by autoinhibition. Current biology : CB. 2003; 13:1335–1340. [PubMed: 12906795]

32. Rath N, Olson MF. Rho-associated kinases in tumorigenesis: re-considering ROCK inhibition for cancer therapy. EMBO reports. 2012; 13:900–908. [PubMed: 22964758]

33. Haak AJ, et al. Targeting the myofibroblast genetic switch: inhibitors of myocardin-related transcription factor/serum response factor-regulated gene transcription prevent fibrosis in a murine model of skin injury. The Journal of pharmacology and experimental therapeutics. 2014; 349:480–486. [PubMed: 24706986]

34. Sisson TH, et al. Inhibition of myocardin-related transcription factor/serum response factor signaling decreases lung fibrosis and promotes mesenchymal cell apoptosis. The American journal of pathology. 2015; 185:969–986. [PubMed: 25681733]

35. Ally MS, et al. Effects of Combined Treatment With Arsenic Trioxide and Itraconazole in Patients With Refractory Metastatic Basal Cell Carcinoma. JAMA dermatology. 2016:1–5.

36. Sekulic A, et al. Pivotal ERIVANCE basal cell carcinoma (BCC) study: 12-month update of efficacy and safety of vismodegib in advanced BCC. Journal of the American Academy of Dermatology. 2015; 72:1021–1026 e1028. [PubMed: 25981002]

37. Vasudevan HN, Soriano P. SRF regulates craniofacial development through selective recruitment of MKL1 cofactors by PDGF signaling. Developmental cell. 2014; 31:332–344. [PubMed: 25453829]

38. Esnault C, et al. Rho-actin signaling to the MKL1 coactivators dominates the immediate transcriptional response to serum in fibroblasts. Genes & development. 2014; 28:943–958. [PubMed: 24732378]

39. Schneider P, et al. Identification of a novel actin-dependent signal transducing module allows for the targeted degradation of GLI1. Nature communications. 2015; 6:8023.

40. Horn A, et al. Hedgehog signaling controls fibroblast activation and tissue fibrosis in systemic sclerosis. Arthritis and rheumatism. 2012; 64:2724–2733. [PubMed: 22354771]

41. Parri M, Chiarugi P. Rac and Rho GTPases in cancer cell motility control. Cell communication and signaling : CCS. 2010; 8:23. [PubMed: 20822528]

42. Jiang P, Enomoto A, Takahashi M. Cell biology of the movement of breast cancer cells: intracellular signalling and the actin cytoskeleton. Cancer letters. 2009; 284:122–130. [PubMed: 19303207]

43. Morita K, Lo Celso C, Spencer-Dene B, Zouboulis CC, Watt FM. HAN11 binds mDia1 and controls GLI1 transcriptional activity. Journal of dermatological science. 2006; 44:11–20. [PubMed: 16887337]

44. Johnson LA, et al. Novel Rho/MRTF/SRF inhibitors block matrix-stiffness and TGF-beta-induced fibrogenesis in human colonic myofibroblasts. Inflammatory bowel diseases. 2014; 20:154–165. [PubMed: 24280883]

45. Wang GY, et al. Establishment of murine basal cell carcinoma allografts: a potential model for preclinical drug testing and for molecular analysis. The Journal of investigative dermatology. 2011; 131:2298–2305. [PubMed: 21833014]

46. Wang GY, Wang J, Mancianti ML, Epstein EH Jr. Basal cell carcinomas arise from hair follicle stem cells in Ptch1(+/-) mice. Cancer cell. 2011; 19:114–124. [PubMed: 21215705]

47. Atwood SX, et al. Smoothened variants explain the majority of drug resistance in Basal cell carcinoma. Cancer cell. 2015; 27:342–353. [PubMed: 25759020]

48. Kuleshov MV, et al. Enrichr: a comprehensive gene set enrichment analysis web server 2016 update. Nucleic acids research. 2016; 44:W90–97. [PubMed: 27141961]

49. Peterson KA, et al. Neural-specific Sox2 input and differential Gli-binding affinity provide context and positional information in Shh-directed neural patterning. Genes & development. 2012; 26:2802–2816. [PubMed: 23249739]

50. Lee EY, et al. Hedgehog pathway-regulated gene networks in cerebellum development and tumorigenesis. Proceedings of the National Academy of Sciences of the United States of America. 2010; 107:9736–9741. [PubMed: 20460306]

51. Vokes SA, Ji H, Wong WH, McMahon AP. A genome-scale analysis of the cis-regulatory circuitry underlying sonic hedgehog-mediated patterning of the mammalian limb. Genes & development. 2008; 22:2651–2663. [PubMed: 18832070]

52. Webster DE, et al. Enhancer-targeted genome editing selectively blocks innate resistance to oncokinase inhibition. Genome research. 2014; 24:751–760. [PubMed: 24443471]

53. Sullivan AL, et al. Serum response factor utilizes distinct promoter- and enhancer-based mechanisms to regulate cytoskeletal gene expression in macrophages. Molecular and cellular biology. 2011; 31:861–875. [PubMed: 21135125]

54. McLean CY, et al. GREAT improves functional interpretation of cis-regulatory regions. Nature biotechnology. 2010; 28:495–501.

55. Noubissi FK, et al. Role of CRD-BP in the growth of human basal cell carcinoma cells. The Journal of investigative dermatology. 2014; 134:1718–1724. [PubMed: 24468749]
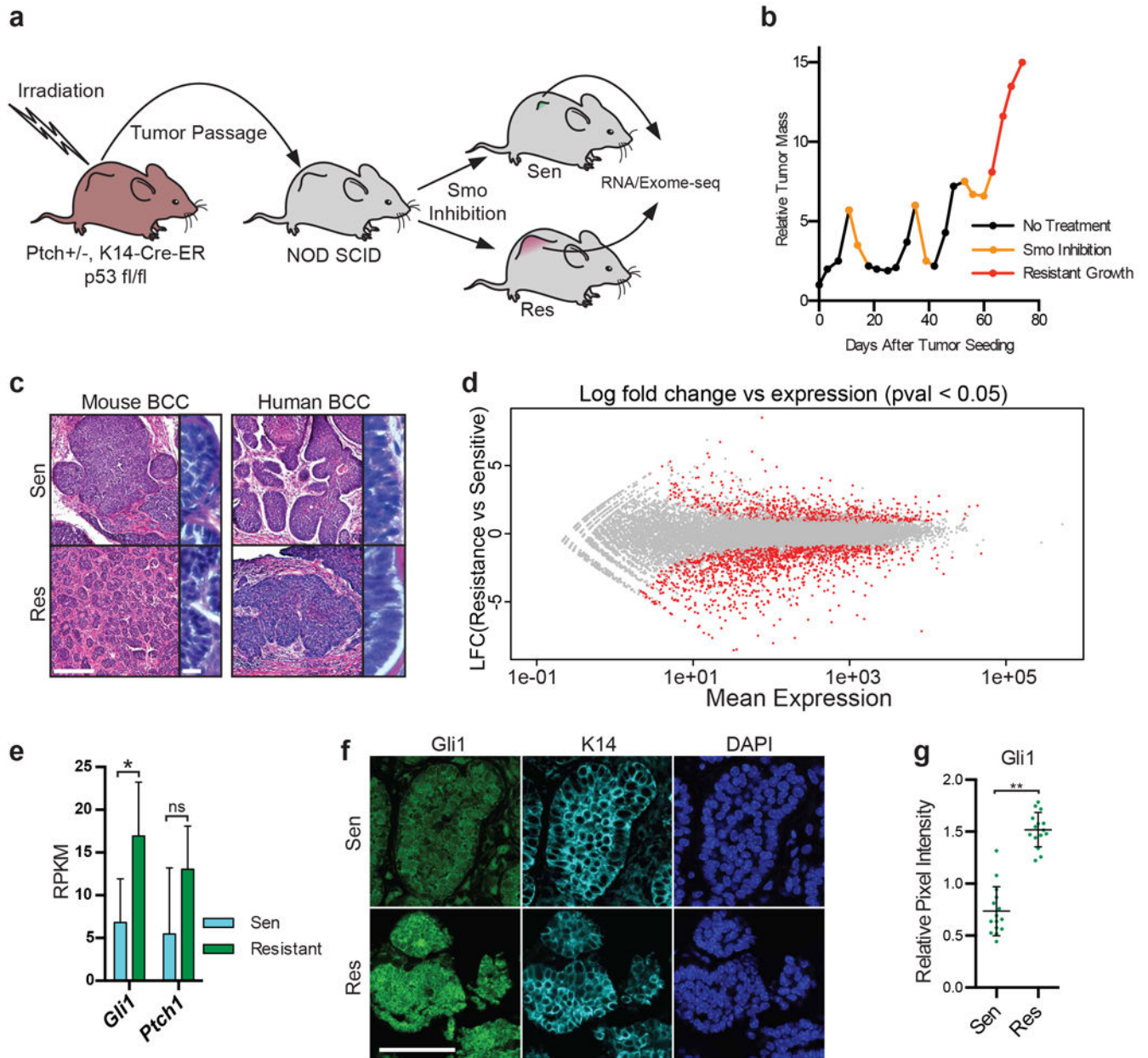
Figure 1. BCC mouse model produces Smo inhibitor-resistant tumors with human tumor characteristics

a, Schematic representation of resistant BCC tumor generation using *Ptch1*+/-, *K14*-Cre-ER, *p53* fl/fl (PTC53) mice. **b**, Representative growth curve illustrating resistant tumor formation after 3 cycles of Smo inhibitor treatment. **c**, Hematoxylin and eosin stain of sensitive and resistant BCCs from mouse and human patient BCCs indicates similar histology. **d**, Genome-wide differential transcript expression sequencing (DE-seq) plot highlights genes with significantly changed expression in resistant versus sensitive mouse tumors. Transcripts with +/- log$_2$ fold change (LFC) in expression and p 0.05 are highlighted in red. **e**, *GLI1* and *PTCH1* mRNA expression obtained from RNA-seq data **d**, in sensitive and resistant

mouse BCCs. Data represents mean from four tumors per condition ± SEM. **f**, GLI1 protein expression indicated by immunofluorescence (IF) staining in mouse sensitive and resistant BCCs. Cytokeratin-14 (K14) stain used to demarcate epithelial-derived BCCs in tissue sections. **g**, Quantification of GLI1 protein expression in **f** by pixel intensity measurements (number of fields measured - n = 15 for each condition). Data represents mean ± SEM. Students t-test used to determine differential expression significance, *P < 0.05, **P < 0.001, NS = not significant. n = 4 for each group in **d** and **e**. n = 15 for each group in **g**.
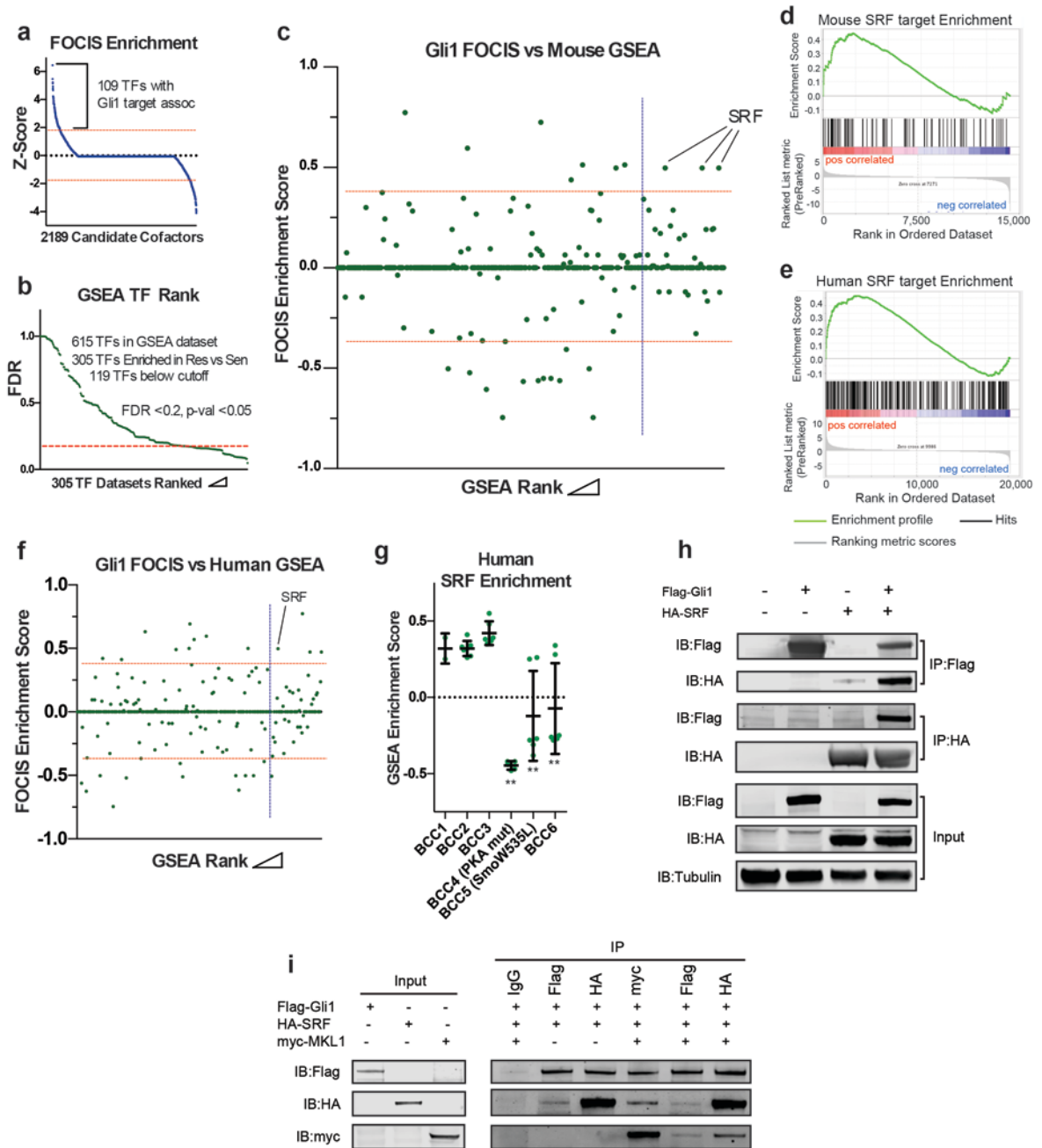
Figure 2. Multicomponent genomic analyses uncover serum response factor as a novel hedgehog cofactor with increased activation in resistant BCCs

a, The feature overlapper for chromosomal interval subsets (FOCIS) algorithm used to highlight putative GLI1 transcriptional co-activators. GLI1 ChIP-seq data was utilized to pattern match transcription factor binding signatures from ENCODE, TRANSFAC, JASPER, Swiss Regulon, HOCOMOCO, and UCSC Conserved TFBS databases. Red lines indicate cutoff for top and bottom 5% of positive and negative enrichment respectively. **b**, Gene set enrichment analysis (GSEA) carried out using the TRANSFAC database for

transcription factor targets (TFT). GSEA utilized to uncover TFs with increased activity in resistant versus sensitive BCCs. Red line indicates the cutoff where false discovery rate (FDR) reaches 0.2 with a p-value of 0.05. c, Multicomponent plot combines FOCIS (**a**) and GSEA (**b**) datasets to uncover serum response factor (SRF) as the top TF enriched in both analyses. Red line indicates cutoff for the top and bottom 5% of FOCIS hits and blue line indicates cutoff for top 10% of GSEA enriched targets. Representative GSEA enrichment plots shown indicating increased activity in mouse (**d**) and human (**e**) resistant BCCs. **f**, Multicomponent analysis using RNAseq from human BCCs reveals SRF enrichment in resistant tumors. **g**, GSEA analysis for SRF in individual human resistant BCCs indicates SRF enrichment only in tumors without activating mutations in canonical HH pathway activators. Unpaired students t-test comparing the average of BCCs 1-3 and BCC4, 5, and 6 individually. **P < 0.001 for SRF GSEA enrichment of indicated sample using all available TRANSFAC datasets. Data represents individual SRF datasets with mean (center line) ± SEM. **h**, Reciprocal co-immunoprecipitation in 293T cells using antibodies against FLAG-GLI1 and HA-SRF. **i**, Inverse co-immunoprecipitation in rabbit reticulocyte extracts using antibodies against FLAG-GLI1, HA-SRF, and myc-MKL1.
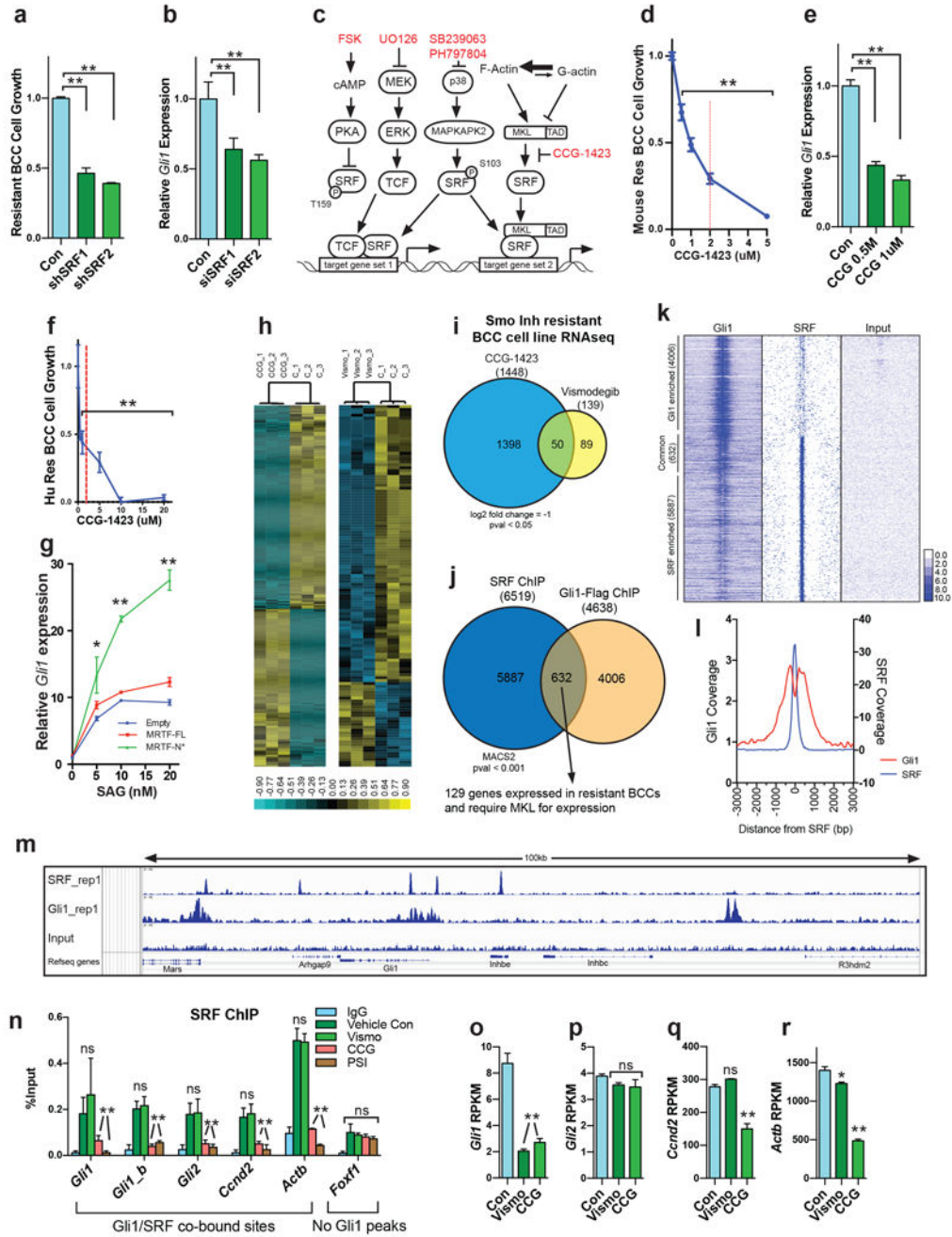
Figure 3. SRF/MKL1 are necessary for resistant BCC growth and potentiate hedgehog pathway activity

a, MTS assay carried out in ASZ001 with stable expression of antisense shRNAs against SRF. **b**, qPCR for *GLI1* in ASZ001 cells with transient SRF knockdown. **c**, Schematic representation of known SRF activating pathways and associated inhibitors. **d**, MTS assay using the MKL inhibitor CCG-1423 uncovers MKL1 as a necessary SRF activator in ASZ001 cells. Data points represent mean MTS absorbance for biological triplicates ±SD. Red line indicates previously reported IC50 for CCG-1423. **e**, Relative expression of *GLI1*

mRNA in response to CCG-1423 treatment. **f**, MTS growth assay carried out in human resistant BCC cells (UW-BCC1) treated with indicated concentration of MKL inhibitor. g, mRNA expression of *GLI1* in NIH-3T3 cells following Smoothened agonist (SAG) treatment in cells expressing full length MKL1 (MKL1-FL) and constitutively-active MKL1 (MKL1-N*). **h**, RNA-seq used to determine differential expression of genes regulated by CCG-1423 (1μM, left panel) and vismodegib (150nM, right panel) in ASZ001 cells. **i**, RNA-seq used to identify overlapped genes downregulated by CCG-1423 and vismodegib. **j**, Chromatin immunoprecipitation followed by sequencing (ChIP-seq) utilized to identify SRF and GLI1 genome-wide binding profiles and overlap within respective genomic peak intervals. **k**, ChIP-seq peak enrichment for common GLI1/SRF bound loci across 6kb genomic regions centered on SRF peaks. **l**, Positional ChIP-seq peak enrichment for SRF relative to GLI1 in ASZ001 cells. **m**, Representation snapshot of local ChIP-seq peak enrichment at the GLI1 genomic locus. **n**, Chromatin immunoprecipitation (ChIP) followed by qPCR using oligos against the 5' untranslated region of *GLI1, GLI2, CCND2, ACTB, and FOXF1*. SRF occupancy is abolished after MKL1 inhibition (CCG-1423) or GLI1 inhibition (PSI) at all tested loci except for FoxF1. **o-s**, RPKM values from RNA-seq data for genes containing differential ChIP occupancy in panel **n**. Data represent mean qPCR fold enrichment over IgG control ±SD. Students t-test (two-tailed) used to determine significance for pairwise observations, $*P < 0.05$, $**P < 0.001$, ns = not significant. All data points represent the mean of triplicates ± SEM. For all ChIP experiments, vismodegib (Vismo), CCG-1423, and PSI were treated at 150nM, 1μM, and 5μM respectively.
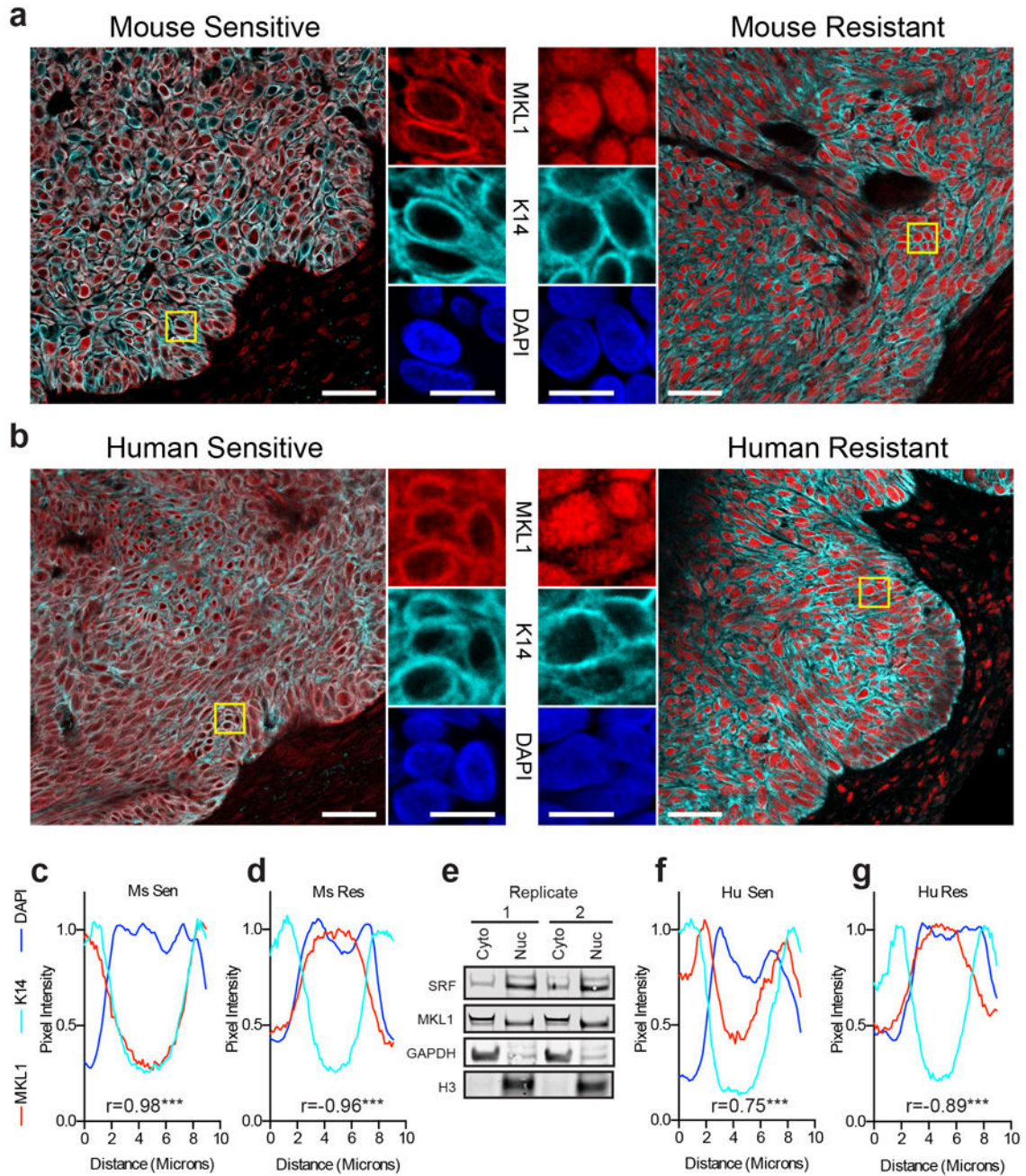
Figure 4. MKL1 accumulates in the nucleus in resistant mouse and human BCCs

Immunofluorescence staining using antibodies against MKL1 and cytokeratin-14 (K14) in mouse (**a**) and human patient (**b**) BCC tumor sections. **c-d** and **f-g**, Compartmental quantification of tumor immunostaining. Positional staining intensity measured using the ImageJ multi-plot particle measure tool. K14 and DAPI used as markers for cytoplasmic and nuclear compartments respectively. n = 16 for resistant and n = 14 for sensitive mouse tumors. n = 24 for resistant and n = 11 for sensitive human tumors. Scale bars = 50μm and 10μm in respective low and high magnification fields. Pearson coefficient (r) used to determine MKL1 staining correlation with K14 (cytoplasmic) staining (***P < 0.001). **e,**

ASZ001 cellular fractionation followed by immunoblotting for SRF and MKL1 highlights nuclear localization.
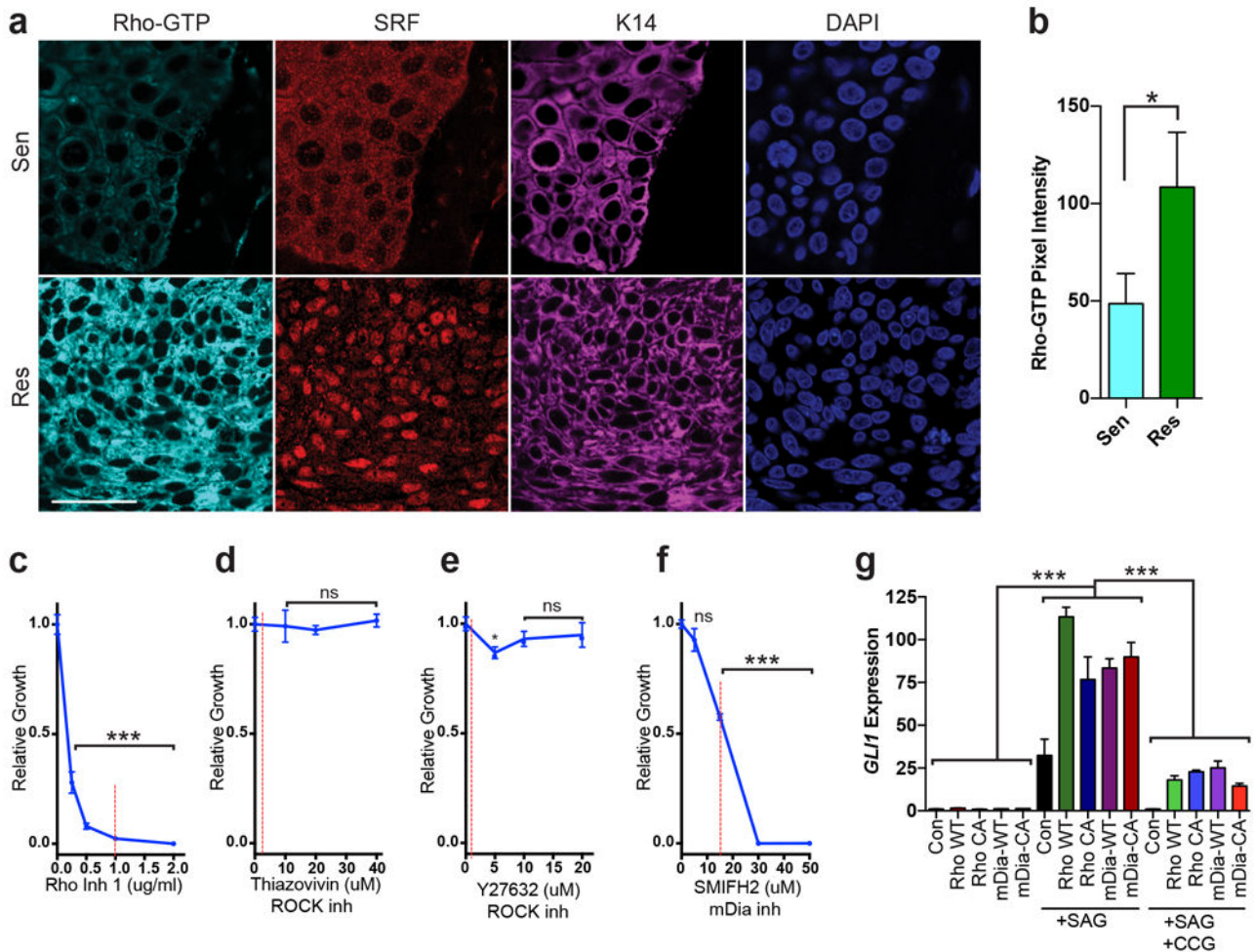
Figure 5. Downstream hedgehog activation requires active Rho/mDia

a, Mouse tumor staining indicates activated Rho (Rho-GTP) in resistant BCC tumor sections. **b**, Quantification of Rho-GTP staining in **a** (*P < 0.05). **c-f**, MTS growth assays in ASZ001 cells treated with inhibitors against Rho (Rho inhibitor I), Rho-associated protein kinase (Thiazovivin and Y27632), and mDia (SMIFH2). Vertical red line indicates previously reported IC50 value. **g**, NIH-3T3 cells expressing wild-type Rho (Rho-WT), constitutively-active Rho (Rho-CA), wild-type mDia (mDia-WT), and/or constitutively-active mDia (mDia-CA). Cells were treated with 20nM SAG for 24hr after indicated transfection. Data points represent mean qPCR induction for GLI1 using technical triplicates ±SD. Students t-test used to determine significance (***P < 0.001) for indicated conditions versus control, SAG treatment, or SAG treatment + CCG-1423. Data represent in **b-g** indicates mean of triplicates ± SEM. Scale bar represents 50μm for images in **a**.
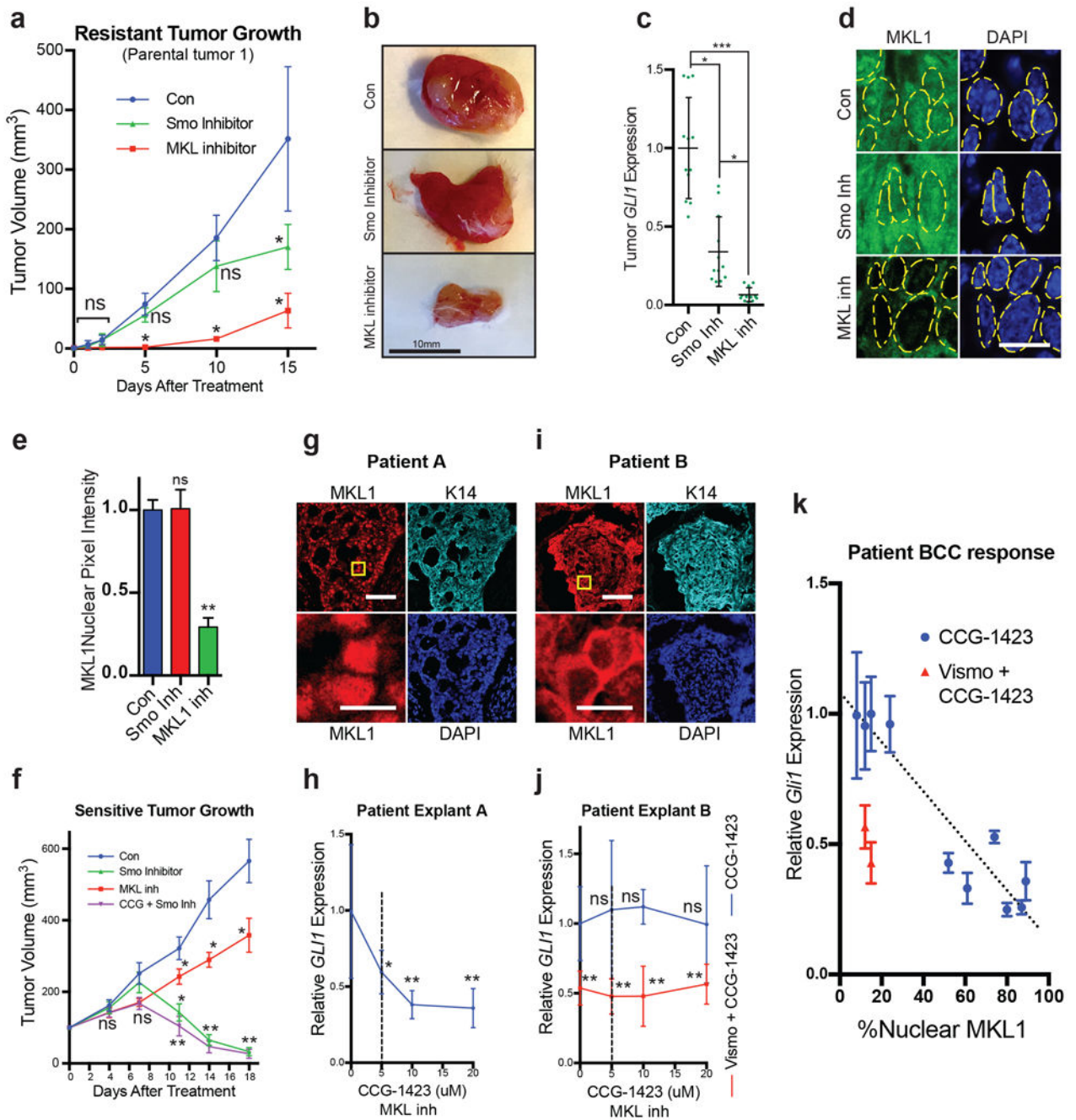
Figure 6. Pharmacological inhibition of MKL1 produces *in vivo* therapeutic response in mouse and human BCCs

a, Resistant BCCs were generated in PTC53 mice by Smo-inhibitor cycling. Parental resistant tumors were passaged twice in NOD/SCID mice and subsequently treated with Smo-inhibitor (vismodegib), MKL inhibitor (CCG-203971), or vehicle control (DMSO "Con") by intraperitoneal injection. Caliper measurements were used to calculate tumor volume at indicated time points. Students t-test used to determine change in tumor volume compared to vehicle control. *P < 0.05, ns=no significant change compared to vehicle

control. n = 4 for each condition, data repeated in Supplementary Fig. 15 using a distinct parental tumor line. **b**, Representative tumors after inhibitor treatment. **c**, qPCR carried out to measure *GLI1* mRNA expression in resistant mouse tumors treated with indicated inhibitors (n = 12 per condition, *P < 0.05, ***P < 0.001). **d**, Immunofluorescence staining for MKL1 indicates cytoplasmic localization in CCG-203971-treated tumor sections. Yellow dotted line included to highlight nucleus in left and right panels. Scale bar represents 10μm. **e**, Quantification of MKL1 nuclear pixel intensity in tumors treated with indicated inhibitor (n = 100 cells per condition, **P < 0.01, ns = not significant). **f**, Drug naïve mouse tumors were passaged from PTC mice into NOD/SCID recipients. Tumors treated with vehicle control (DMSO), CCG-203971 (i.p. 100mg/kg), Smo inhibitor (XL139, oral gavage 25mg/ kg), or indicated combination. Caliper measurements were used to calculate tumor volume at indicated time points. (*P < 0.05, **P < 0.01). **g**, Representative immunofluorescence staining of 10 consecutive fresh surgical specimens highlights variable nuclear localization of MKL1 in human advanced BCC tumor explants. **h**, qPCR from treated tumor with nuclear MKL1 shown in **g**, reveals MKL1 inhibition causes reduced GLI1 expression (*P < 0.05, **P < 0.01 – t-test compares individual data points versus vehicle control). **i**, Representative immunofluorescence field highlighting cytoplasmic accumulation of MKL1 in human advanced BCC tumor explants. **j**, qPCR reveals MKL1 inhibition has minimal GLI1 response in the same tumor shown in **i**, however, 1μM Vismodegib (Vismo) treatment produces a robust GLI1 response (**P < 0.01 – t-test compares individual data points versus vehicle control). **k**, Percentage of cells containing nuclear accumulation of MKL1 (x-axis) was obtained for all drug-treated human advanced BCC tumors specimens collected (n = 10). qPCR highlights GLI1 response to MKL1 inhibition (CCG-1423 – blue dots) or Smo inhibition (Vismodegib – red triangles). Best fit linear regression line (black dotted line) shown to highlight the relationship between nuclear MKL1 and GLI1 response following MKL1 inhibition. Data represented in **a, c, e, f, h, j**, and **k** indicate mean ± SEM. For **g** and **i**, scale bars = 50μm and 10μm in respective low and high magnification fields.